Research Square

Preprints are preliminary reports that have not undergone peer review.
They should not be considered conclusive, used to inform clinical practice,
or referenced by the media as validated information.

Simulating Ground Vibrations Induced by Hypothetical Large Scale Slope Collapse Using Unified Geomechanical and Seismic Methods

João Pedro Delveaux

joaopedrodelveaux@gmail.com

Universidade Federal de Ouro Preto

Rodrigo Peluci Figueiredo

Universidade Federal de Ouro Preto

Claus Naves Eikmeier

Michael Afanasiev

Research Article

Keywords: site-specific ground motion, seismic wave propagation, MPM-SEM, run-out, large deformation geomechanics

Posted Date: November 26th, 2026

DOI: https://doi.org/10.21203/rs.3.rs-11448330/v1

License: This work is licensed under a Creative Commons Attribution 4.0 International License.
Read Full License

Additional Declarations: No competing interests reported.

Simulating Ground Vibrations Induced by Hypothetical Large Scale Slope Collapse Using Unified Geomechanical and Seismic Methods

João Pedro Delveaux[a], Rodrigo Peluci Figueiredo[a], Claus Naves Eikmeier[b], Michael Afanasiev[c].

Correspondence Author
João Pedro Delveaux
a - Center for Geotechnics, School of Mines, Federal University of Ouro Preto, MG – Brazil
City: Ouro Preto
Country: Brazil
E-mail: joaopedrodelveaux@gmail.com

Authors:
Rodrigo Peluci Figueiredo
a - Center for Geotechnics, School of Mines, Federal University of Ouro Preto, MG – Brazil
City: Ouro Preto
Country: Brazil
E-mail: rpfigueiredo@ufop.edu.br

Claus Naves Eikmeier
b - Tetra Tech South America, MG - Brazil.
City: Belo Horizonte
Country: Brazil
E-mail: eikmeiercn@gmail.com

Michael Afanasiev
c - Mondaic Ltd., CH
City: Zürich
Country: Switzerland
E-mail: michael.afanasiev@mondaic.com

Abstract:

This work introduces a fully deterministic, integrated multi-method framework designed to model a site-specific seismic wave propagation originating from a hypothetical future massive non-tectonic slope failure. Aimed to simulate the ground vibrations generated by a potential, abrupt ten-million-ton collapse within an open-pit mine, the framework characterizes the seismic source by coupling ground based interferometric radar monitoring with macroscopic deformation data. These datasets inform a three-dimensional stress-strain failure analysis to define representative seismic source surfaces, which subsequently drive 3D numerical modeling via the Material Point Method (MPM) to calculate the dynamic contact forces

[a] Center for Geotechnics, School of Mines, Federal University of Ouro Preto, MG – Brazil

...

resulting from mass displacement. Next, the Spectral Element Method (SEM) is deployed to simulate mechanical wave propagation through a real geologic medium, accounting for all geometric and elastic wave effects except for intrinsic attenuation. This interconnected computational pipeline bridges large deformation geomechanics with high fidelity wave propagation; unlike existing literature that predominantly focuses on earthquake induced landslides via a SEM to MPM approach, this research introduces a novel inverse pathway (MPM to SEM) where the mining induced failure acts as the primary seismic source. By embedding complex 3D topographies, multi-layered geological interfaces, and heterogeneous lithological variations directly into the elastic model, the framework accurately captures site-specific phenomena, such as surface wave amplification, geometric spreading, and structural attenuation, up to a high frequency limit of 15 Hz. Ultimately, the model successfully quantifies localized ground motion variations in terms of peak velocity, peak acceleration, and complex waveforms across the domain, offering a robust tool for future risk assessment in nearby critical infrastructure.

Key words: site-specific ground motion; seismic wave propagation; MPM-SEM; run-out; large deformation geomechanics.

1. Introduction

Following recent cases of massive slope failures (Pankow *et al.,* 2014), the geotechnical community has developed predictive modeling and stability assessment frameworks aimed at evaluating the stability of geotechnical structures under a range of situations envisioned through risk analyses. A possible scenario capable of inducing slope failure and causing damage to critical infrastructure is through seismic wave propagation. Standard literature frameworks predominantly model seismic vibrations and subsequently their impacts on slopes (Feng *et al.,* 2022). Conversely, the objective of this work is to model ground vibrations generated directly by a possible massive slope collapse, in the context of proximity of civil and geotechnical structures.

To evaluate wave propagation from a given source, it is possible to construct simulations, termed Path Models by Kramer and Stewart (2024). These simulations consider various effects, including geometric spreading, wave amplification and attenuation, and the reflections and refractions occurring at the interfaces of distinct materials from the source to the site of interest, namely an alternative to probabilistic studies is modeling aimed at capturing local seismic effects within a fully deterministic framework (Zhao *et al.,* 2022). These effects are defined by characterizing the seismic source in terms of force and its conversion into waveforms, the specific characteristics of the materials composing the propagation medium, and the local topography.

Given the current state of conservation of the slopes in a specific open pit mine, there was a need to evaluate the potential impact of a hypothetical abrupt mass failure in terms of seismic wave propagation simulation. The seismic modeling was conducted in the region of a mine located in Brazil, in a region known for containing large iron ore reserves, known as the Iron Quadrangle.

The slopes, outlined in orange in Figure 1, are defined as the seismic source, involve a mobilized volume of approximately 10 million tons. This pit mine features an elliptical geometry, with a major axis of approximately 2.2 kilometers and a minor axis of 1.1 kilometers. Outlined in red

and blue are the embankment and the reservoir of a tailings dam, respectively. The tailings dam has an approximate volume of 9 million cubic meters of disposed material. Between the pit and the dam, waste material disposed of is marked in yellow. The white line represents a federal concession railway containing two viaducts, shown in blue.

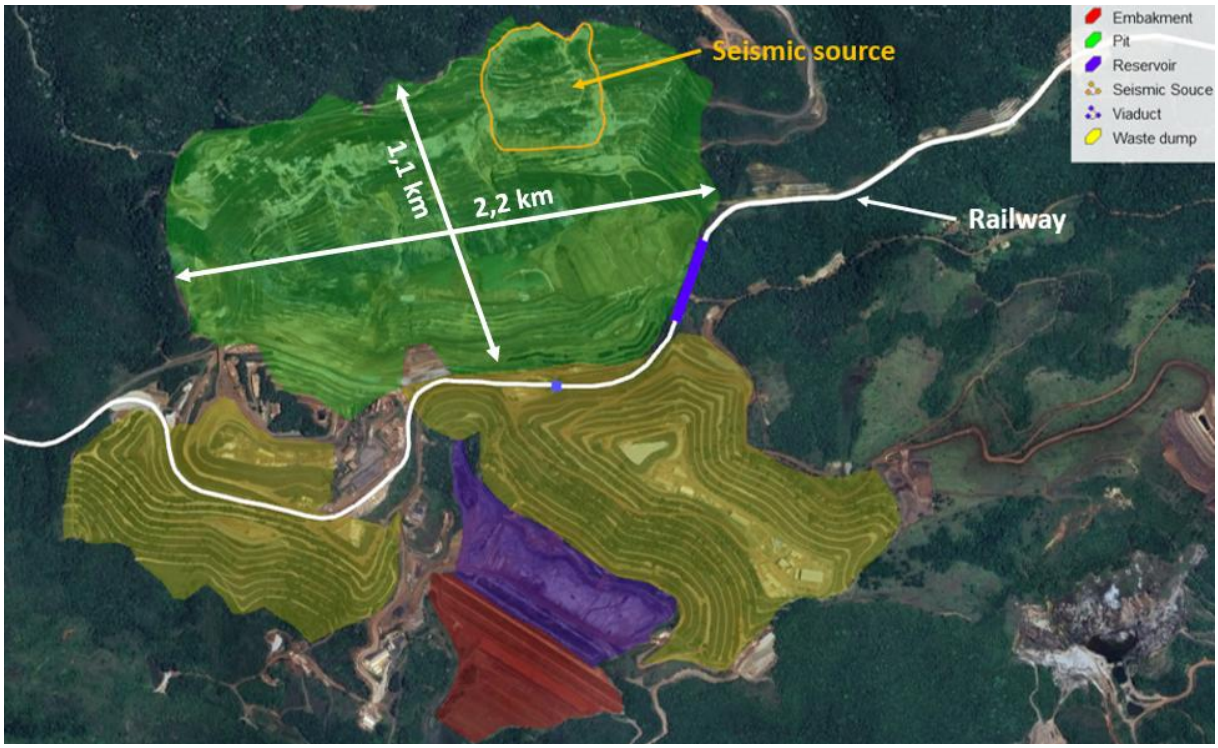


Figure 1: spatial representation physical medium model used in the wave propagation study.

2. Methods

The seismic modeling considered herein focused on the surrounding region of the seismic source, where wave propagation was simulated. In this context, the seismic source characterization was performed by determining the main characteristics of the failure, such as the geometry of the failed mass, its volume, and the subsequent modeling of its abrupt collapse. Based on the understanding of the flow characteristics, the contact forces existing on the failure plane and the remaining mass were estimated and the wave propagation was simulated.

2.1 Contact Forces

Among the solutions developed to model large post-collapse deformations, necessary to obtain the contact forces of de run-out, are those combining the solution of the momentum equations at specific locations with the use of discrete particles, effectively integrating Eulerian and Lagrangian descriptions. Within this context, the Material Point Method (MPM) emerges as an ideal framework by employing a dual-system approach, material points and a background mesh, to track the model's behavior throughout the simulation (Zhao *et al*., 2022; Sulsky *et al*., 1994).

The MPM computational cycle is primarily divided into two phases: Lagrangian and Eulerian. In the Lagrangian phase, the particles move together with the mesh, which deforms to provide a finite element discretization of the material domain. This allows the momentum equation to be solved using the standard finite element formulation. Since the mesh acts as an updated Lagrangian framework during this stage, the convective term typical of pure Eulerian

formulations is eliminated. In the Eulerian phase, the mesh is simply reset to its original configuration within the time step to account for the convective term, while the particles remain in their updated positions (Eikmeier *et al*., 2024; Zhao *et al*., 2022; Zhang *et al*., 2017).

According to Zhao *et al.* (2022), the mathematical formulations of the Material Point Method, in a simplified form, consist of calculating the nodal momentum *f* at the nodes based on the calculation of internal forces (f^{int}) governed by the stress state and external forces (f^{ext}), which represent the boundary conditions of the problem.

$$f = f^{int} + f^{ext}$$

where $f^{int} = -\sum_p S_{Ip,j}\ \sigma_{ijp} \frac{m_p}{p_p}$ and $f^{ext} = \sum_p S_{Ip}\ m_p b_{ip} + \sum_p S_{Ip}\ \frac{m_p}{p_p}\ t_{ip} h^{-1} \frac{m_p}{p_p}$

since σ_{ijp} denotes the stress state of point p, p_p is the density of the material point p, m_p is the mass of particle p, b_{ip} is the body force, t_{ip} represents the boundary condition and h is the layer thickness. Thus, it becomes possible to simulate large deformations and the run-out of the failed material, providing the time series of contact forces that act as the seismic trigger**.**

2.2 Elastic Wave Propagation

Once the contact forces are obtained as sum of internal forces plus external forces obtained at nodes of mesh from MPM, the process moves to the propagation of the elastic waves generated by this impact through the rock mass, by applying the wave propagation equation in a continuous and isotropic medium. One of the possible formulations of the elastic wave equation in an isotropic medium can be expressed by the following equation (Fichtner, 2011; Shearer, 2009; Slawinski, 2003):

$$\rho \frac{\partial^2 u}{\partial t^2} = \nabla\lambda\psi + \nabla\mu(\nabla u + (\nabla u)^2) + (\lambda + 2\mu)\nabla\psi - \mu\nabla \times \Omega + \rho g$$

In this equation ρ is the density, u is the displacement, t is time, g is gravity, ∂ is s the partial derivative, ∇ is the gradient, $\nabla.$ is the divergence, ∇^2 is the Laplacian, and $\nabla \times$ is the curl. When the divergence of the displacement vector ($\nabla.u$), it was represented in the equation above by ψ, and the curl of the displacement vector, ($\nabla \times u$) by Ω.

The application of the elastic wave propagation equation in the medium from a given source was modeled using the Spectral Element Method (SEM). This method applies numerical procedures to obtain accurate solutions for spatial derivatives and offers geometric flexibility for working with complex topographies. The advantage of this method lies in its use of high-degree polynomials to solve equations related to the physical position of an element. This enables smooth and precise solutions, as the error decreases exponentially with the polynomial degree. Thus, it becomes possible to model seismic wave propagation in a complex and extensive geometry, using irregular and adjustable meshes in terms of shape, orientation and size with significant savings in computational power (Zheng *et al.,* 2019; Igel, 2017; Komatitsch e Tromp, 1999).

In this seismic modeling, attenuation due to geometric spreading and scattering was considered. Attenuation corresponds to the decay of vibration amplitudes as a function of the increased

source-receiver distance and the characteristics of the propagation medium. That is, how parameters vary in space and the order of magnitude of these variations. The combination of attenuation phenomena results in seismic wave propagation models that are more accurate to reality.

Geometrical spreading produces attenuation as a result of energy scattering from a source. The initial energy released in seismic waves propagates along the increasing area of the wavefronts, which implies a loss of energy per unit area, resulting in the decrease of wave amplitudes. It has an essentially geometric characteristic and is affected by material properties and wave frequency.

Attenuation by the scattering effect occurs through the redirection of energy and can lead to a reduction in wave amplitude without the dissipation of elastic energy. It is a result of the acoustic impedance differences of the materials through which the wave travels and increases with higher frequencies. Scattering tends to disorganize a wavefield through the reflections and refractions that occur at the boundaries of heterogeneities. Intrinsic attenuation, which corresponds to the decrease of the seismic signal due to internal friction, was not included in this modeling (Kramer e Stewart 2024, Ammon *et al*., 2021; Igel, H. 2017, Aki and Richards, 2002).

3. Physical Model and Boundary Condition

The study area is characterized by lithological heterogeneity, typically composed of pre-Cambrian metamorphic rock sequences and Cenozoic rocks whose mechanical properties dictate the propagation velocity of P (primary) and S (secondary) waves. To construct the physical medium for wave propagation, a model was developed based on correlations between the lithologies present in the geological model of the mine and their correspondence with geophysical measurements. The existing lithologies were correlated with density ρ, P wave velocity, and S wave velocity measurements.

The physical model used is composed of 84.461.854 points, each of with associated V_p, V_s and ρ values. To generate a regular grid model necessary for processing, the initial model was divided into 239 layers, each corresponding to a specific depth. Since it contains all possible x and y coordinate variations, the deepest layer was chosen as the reference for the number of points each layer should contain. Thus, a regular model with dimensions of 743 x 859 x 239 (x, y, z) meters was obtained (Figure 2).

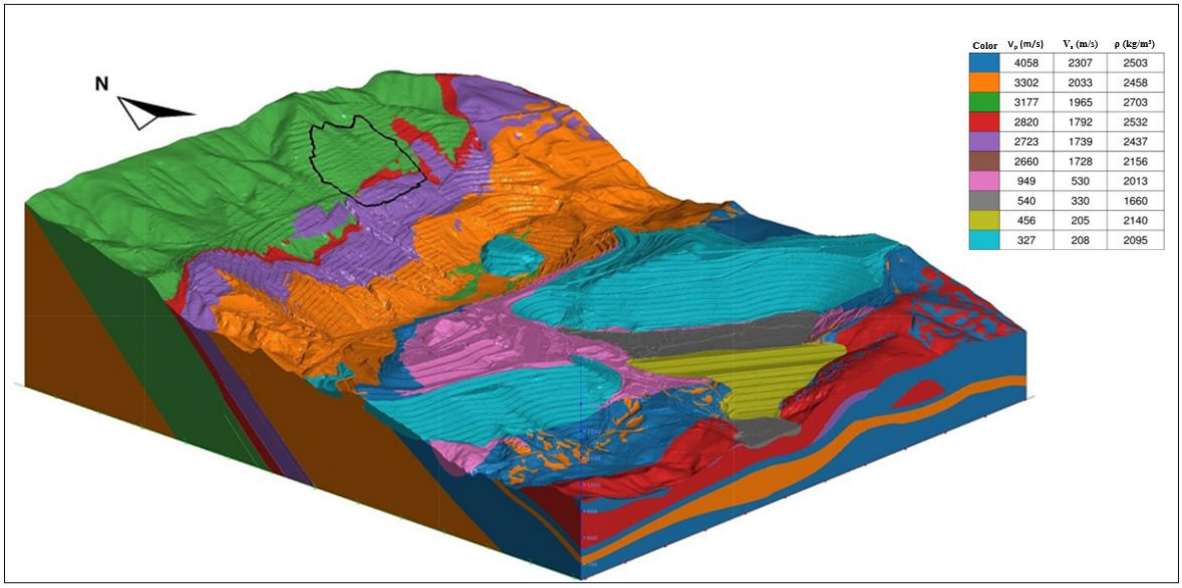


Figure 2: physical medium model used in the wave propagation study. The seismic source is delimited by the black polygon.

3.1 MPM Boundary Condition

The Material Point Method was implemented using the MPM-PUCRio code (Fernandez, 2020), written in C++. The resolution scheme and the updating of displacements and stresses were configured using the Modified Update Stress Last (MUSL) method. During the time-step integration cycle, the algorithm maps data from Particle-to-Grid (P2G) and back from Grid-to-Particle (G2P). The sequence of these operations defines the numerical scheme employed. In the Update Stress Last (USL) algorithm, nodal forces and grid velocities are updated first; subsequently, particle positions and velocities are corrected, and finally, the strain rate is calculated to update the stress tensor. The Modified Update Stress Last (MUSL) scheme is a variation of USL introduced by Nairn (2003) to enhance numerical stability and mechanical energy conservation.

The internal integration time increment was constrained by the Courant–Friedrichs–Lewy (CFL) stability condition, which governs the maximum stable time step (Δt) suitable for explicit integration schemes. An output interval of 0.01 s was defined for recording computational results.

The initial stress state was established via a dynamic relaxation procedure. In this preliminary stage, geostatic loading was applied across all materials, determining stress fields from elastic vertical stresses. Subsequently, the constitutive model was updated to an elastoplastic regime to define the initial induced stresses. Throughout this procedure, the domain was treated as a continuum, preventing the premature development of failure surfaces. Regarding boundary conditions, the model base was fully fixed (zero-displacement constraint), whereas the lateral boundaries were restricted solely in the normal direction to the plane, allowing free vertical movement. The top surface remained unconstrained. The Figure 3 below illustrates the initial stress state employed as well as the spatial extent of the model.

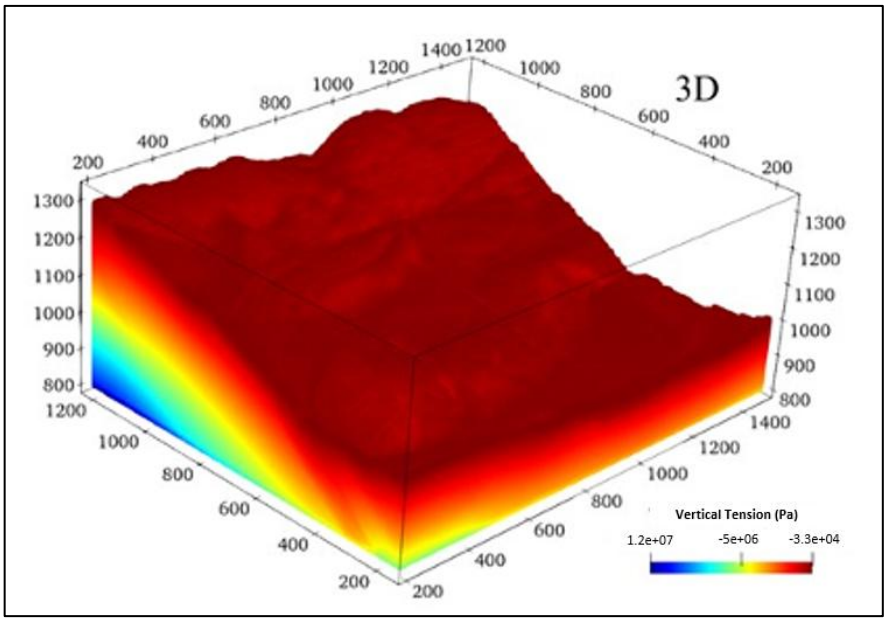


Figure 3: initial state of stress and modeled spatial extent. Negative values indicate compression.

3.1 Topography Modeling

To generating the computational mesh for the SEM simulations, the geological and topographic inputs required additional pre-processing. First, model values were "flooded" vertically from the irregular upper surface to a common elevation, completing the rectangular model volume and enabling efficient interpolation of the three-dimensional material fields onto the degrees of freedom within each element.

The topography was then interpolated onto the same horizontal grid as the geological model using a Clough–Tocher scheme. Gaussian smoothing kernels with standard deviations of two grid points for the topography and four grid points for the material fields were applied before both datasets were horizontally subsampled by a factor of two. This limited smoothing was intended to preserve the principal topographic and lithological variations while suppressing very small-scale features that could produce poorly shaped or excessively small elements, impose a prohibitively small stable time step, and make the simulations computationally infeasible.

Second-order Lagrange interpolation was used to represent the material fields within each element, whereas fourth-order Gauss–Lobatto–Legendre (GLL) polynomials were used to approximate the wavefield. Local mesh-refinement and coarsening policies ensured a minimum resolution of one fourth-order spectral element per wavelength at the maximum frequency of the simulation, corresponding nominally to five GLL solution points per wavelength in each spatial direction.

3.3 SEM Boundary Condition

In the simulated seismic wave propagation scenario, a maximum frequency limit of 15 Hz was considered, due to the available computational power and also the fact that high frequencies tend not to propagate over long distances (Gualtieri e Ekström, 2012). Standard absorbing

boundary conditions used in seismic-wave simulations approximate the radiation of propagating waves into an unbounded exterior domain, but generally do not perform well in the very-low-frequency and static regimes.

For simulations targeting frequencies below 5 Hz, the fisical model was first extended by 1 km laterally and downward. Within this transition region, parameters (Vp, Vs, and density) were tapered smoothly from their values at the edge of the site model toward their respective median values. The domain was then extended by a further 9 km using these constant median properties, resulting in a total extension of 10 km in every direction except through the free surface. A homogeneous Dirichlet condition was applied at the outer boundaries of the mesh, fixing displacement to zero sufficiently far from the source. Sponge layers (Kosloff and Kosloff, 1986) occupied the outermost 9 km to attenuate finite-frequency waves before they reached the fixed boundary.

This hybrid treatment was adopted to accommodate both the gradual spatial decay of the quasi-static displacement field and the radiation of propagating waves: the extended domain and distant Dirichlet condition controlled the static response, while the sponge layers suppressed artificial finite-frequency reflections.

A separate configuration was constructed for the 5–15 Hz band, in which the model was extended by only 1 km before Clayton–Enquist absorbing boundary conditions (Clayton and Engquist, 1977) were applied. This provided at least approximately one wavelength of separation at 5 Hz between the sources and receivers in the region of interest and the absorbing boundaries, without requiring higher-frequency waves to be resolved throughout the complete 10 km extension. Because this configuration was intended for analysis above 5 Hz rather than for estimation of the quasi-static response, it did not require the distant homogeneous Dirichlet boundary used in the low-frequency model.

Within each spectral element, the wavefield was represented using fourth-order GLL polynomials, corresponding to 125 spatial degrees of freedom per element. Time integration was performed using an explicit second-order Newmark scheme, with the stable time step determined automatically from the mesh geometry and local material properties. Simulations were run for a suficiente duration to capture both the passage of the radiated wavefield through the region of interest and the longer-period response of the source.

4. Seismic Source Characterization

The pit of this mine began to be developed in the 1980s with the objective of extracting iron ore. Mining operations were finalized in 2016, when the pit reached its final configuration. In 2019, a failure has developed in the mine pit with accumulated deformations of metric magnitude which, until the conclusion of this work, remains in progress. Figure 4 shows the region during a period preceding the onset of the failure.

To monitor displacement leading up to failure, methods such as ground based interferometric radar are used. The radar is configured to take a line-of-sight (LoS) displacement measurements every 2 minutes and report an instantaneous velocity based on a 1440-minute moving average. The data collected via interferometric radar between 2019 and 2025 indicate an association between intense rainfall events and displacements, where the higher the cumulative rainfall, the

greater the displacements and, consequently, the movement velocity.



Figure 4: photographic record of the region where the seismic source was subsequently established.

In the displacement and velocity graphs shown in Figure 5, it is noted that during the rains of January 2022, the monitoring system recorded instantaneous velocities of up to 1.293 mm/day, resulting in a displacement of approximately 4,2 meters in about one week. In periods of low rainfall, notably observed between May and September, the observed displacements and instantaneous velocities are centimetric, on the order of 2 cm/month.

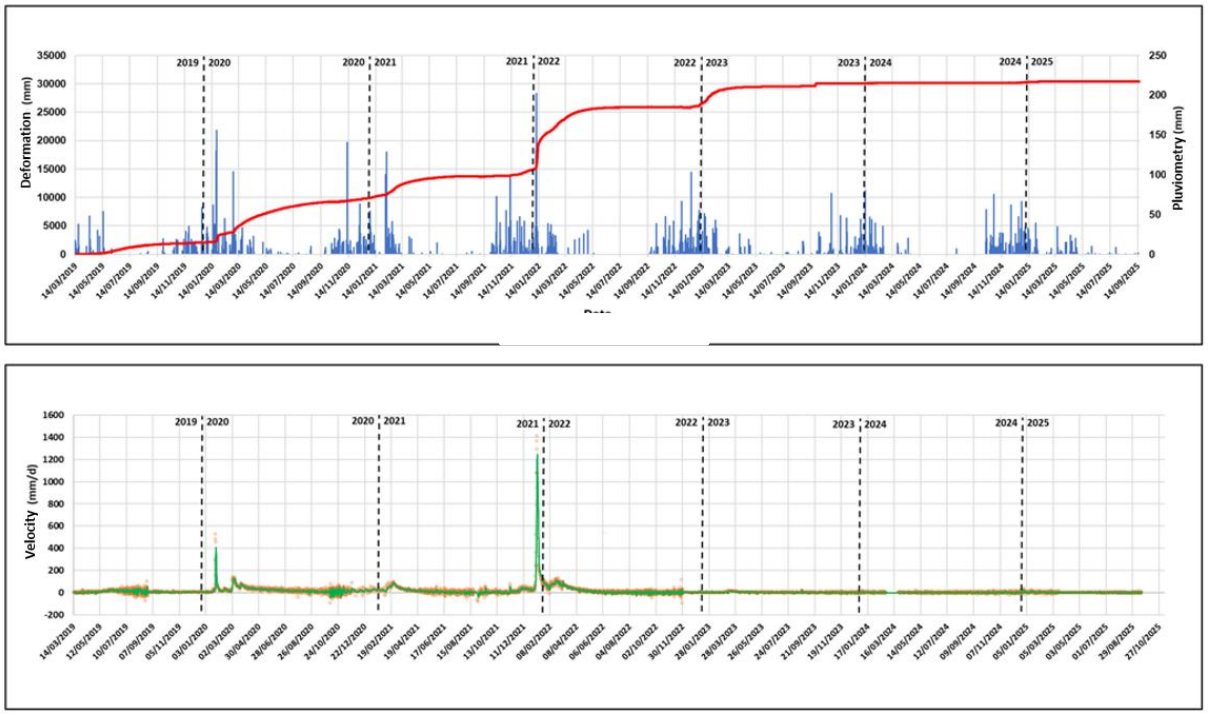


Figure 5: displacement (red) and velocity (green) graphs associated with rainfall events (blue bars).

Visually, it is possible to notice, by observing the photograph shown in Figure 6, taken in 2026, the evolution of the deformation in a well-defined region. It can be observed that a failure plane developed along the rupture boundaries, with the consequent sectioning of the benches in the lateral portions, the formation of a failure plan in the upper portion, and a bulging of the slopes in the lower portion.



Figure 6: photo indicating the current condition of the rupture modeled as a seismic source.

Based on field evidence, a 2D stability analysis was carried out using Rocscience's Slide2 software, version 9.026, which applies the limit equilibrium method. Figure 7 shows the location of the analyzed section in green.

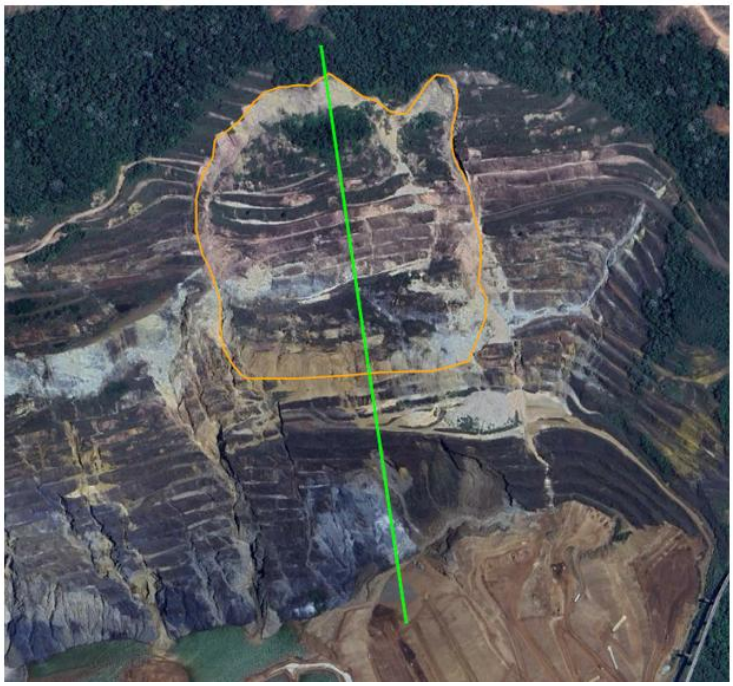


Figure 7: indication of the location, in plain view, of the analyzed section (green).

The material strength parameters were calibrated to obtain a failure surface a Factor of Safety equal to 1. The Mohr-Coulomb strength parameters calibrated, considering the back-analysis of the failure, was applied in the stability analysis are presented in Table 1.

Material Name	Color	Unit Weight (kN/m3)	Sat. Unit Weight (kN/m3)	Cohesion (kPa)	Phi (deg)
BIF Nova Lima		29	32	350	36
Xisto Nova Lima II		27	32	350	36
Xisto Nova Lima III		25	27.5	250	30
Xisto Nova Lima IV		20	22	100	25
Xisto Nova Lima V		17	19	70	23
Xisto Dolomítico Nova Lima II		27	32	350	36
Xisto Dolomítico Nova Lima III		25	27.5	250	30
Xisto Dolomítico Nova Lima IV		20	22	100	25
Quartzito Moeda III		26	28.5	250	40
Quartzito Moeda IV		24	26.5	100	38
Filito Batatal IV		21	23	100	30
Filito Batatal V		18	20	20	28
Filito Transição V		18	20	20	28
Itabirito Friável Dolomitico V		20		80	38
Itabirito Semi-compacto Dolomítico		21	22	27.5	41
Itabirito Compacto		30	33	250	40
Hematita Compacta IV		30	33	120	43
Talco Xisto V		18	20	40	25
Pilha de Estéril		18	20	5	26
Plano de Falha (Espelho)		20	22	0	23

Table 1: Pit strength parameters used in stability analysis following back-analysis.

Simultaneously with the calibration of the strength parameters, was determine the cross-sectional geometry of the failure surface to ensure it was consistent with the failure surface observed. Based on these premises, a failure surface was modeled with a biplanar geometry, featuring an entry along a vertical plane inclined at 45° and an exit along a basal plane with an inclination of 12°, as shown in Figure 8.

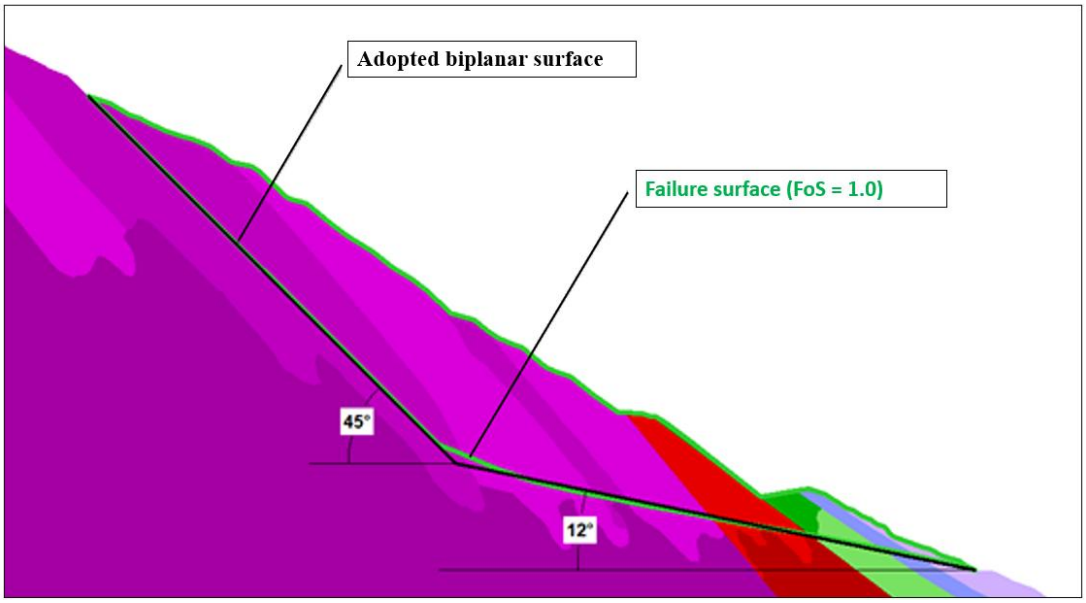


Figure 8: definition of the failure geometry based on 2D stability analysis.

Considering the three-dimensional geological model of the mine, it was possible, based on the 3D analyses, to define the approximate volume of a hypothetical collapsed mass at about 3.2 million m³ or approximately 10 million tons. Incorporating the information obtained in the previous stages, an assessment of the collapsed mass run-out was performed through a 3D analysis of the seismic source, applying the Material Point Method (Eikmeier, C. N *et.al* 2021).

The contact interaction between bodies, governed by Coulomb's friction law, was implemented through a multi-material approach based on nodal velocity fields. Using this differential search algorithm, when velocity fields corresponding to distinct bodies share a common node and exhibit relative motion consistent with contact, velocity and momentum corrections are applied at the nodes, restricting the tangential frictional force component as a function of the normal force and the adopted coefficient of friction.

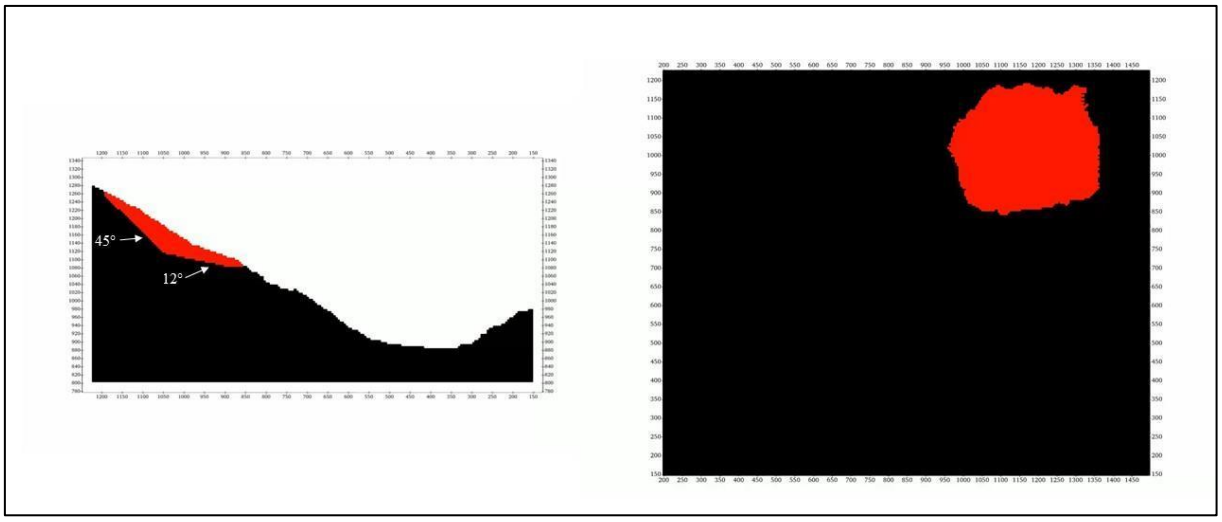


Figure 9: failure modeled in profile and plan views.

The basal friction coefficient (μ), derived from Coulomb's friction law, where calculated based on this equation, $\mu = \tan(\phi)$ where ϕ is coefficient of friction. The basal friction coefficient was applied at the interface between the rupture and the remaining mass, enabling the simulation of the complete collapse of the failed mass toward the bottom of the pit and consequently, the generation of the seismic source. The basal friction coefficient value that enabled the collapse of the failed mass was μ = 0,150. The spatial-temporal results of the rupture are shown in Figure 10.

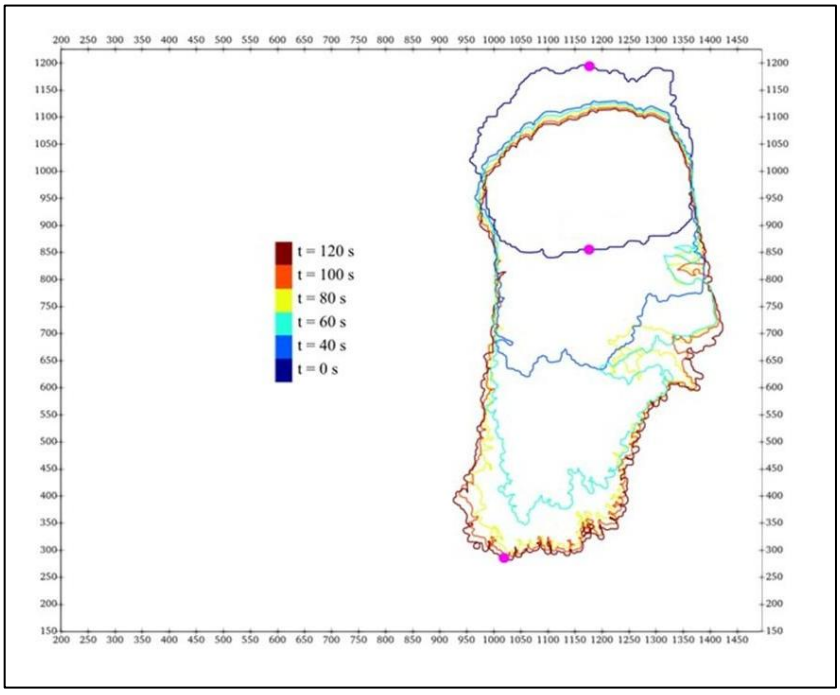


Figure 10: record of the spatial-temporal evolution of the rupture collapse from a plan view perspective.

The approximate boundaries of the failed mass before and after the collapse simulation are shown in the image below (Figure 11).



Figure 11: aerial image illustrating the approximate boundaries of the failed mass before (orange) and after the collapse simulation (red).

The MPM numerical model used in this modeling consisted of 3.6 x 10^6 material points and 1.1 x 10^6 computational nodes. The seismic source is obtained here in terms of the contact force between the collapsing mass and the remaining mass. The simulation results provide the temporal record of the contact force at all points in the numerical model. For each time step, information is provided regarding the coordinates of each contact point and the three-dimensional components of the contact force.

The seismic sources used for wave propagation modeling were calculated based on the mass movement definition, considering the rupture material as elastoplastic and the remaining material as elastic. In the seismic modeling, the medium, excluding the rupture itself, is considered elastic. Thus, the equations of elasticity can be applied to wave propagation.

By compiling the contact forces between the collapsing mass and the pit surface, the seismic sources are obtained. Due to the computational impossibility of inputting a very large number of point sources in the seismic modeling process, the sources were obtained by summing the grid forces contained within non-overlapping cubes with 80 meters sides. In this way, it was possible to consider all forces involved in the hypothetical rupture scenario, resulting in 71 seismic sources. Figure 11 shows the locations of all sources used during the seismic modeling, identified by their respective numbers. For each region delimited by the yellow mesh, the figure shows the maximum resultant force obtained throughout the entire simulation.

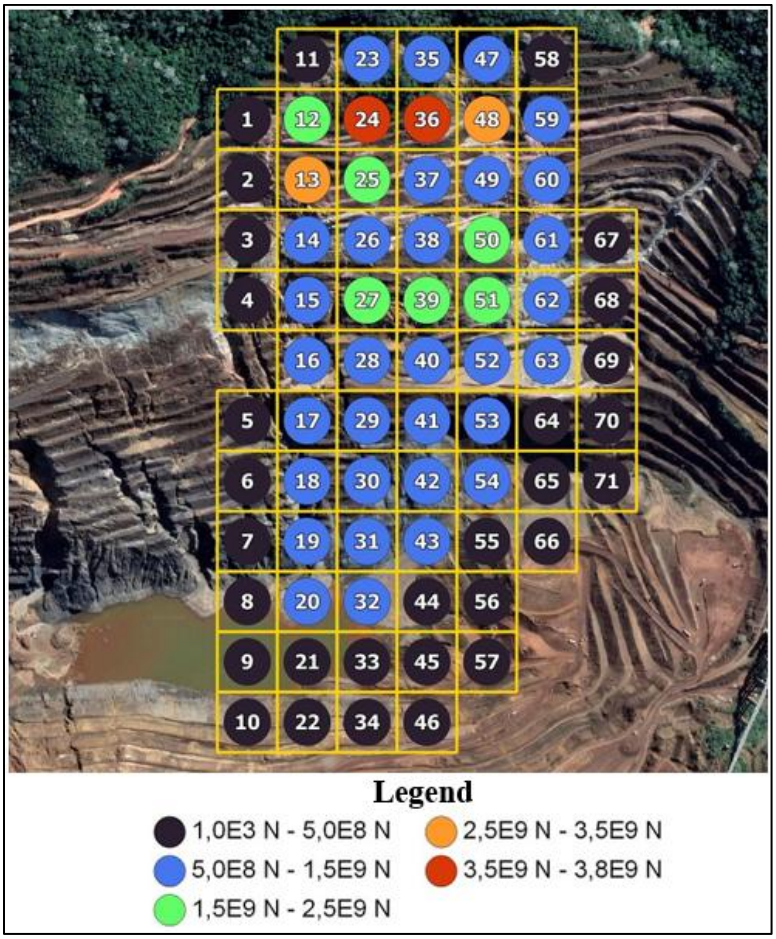


Figure 12: locations of the 71 sources used during the seismic modeling.

5 Seismic Modelling Results

Based on the definition of the seismic sources, the modeling process was carried out by applying the general wave propagation equation in an elastic medium using the Spectral Element Method (SEM). In the simulated seismic wave propagation scenario, a maximum frequency limit of 15 Hz was considered. To study the seismic wave propagation in greater detail, locations of interest were defined within the study area where virtual sensors were placed at specific points. Some of these sensors were allocated at depth. This made it possible to store full waveforms in synthetic seismograms throughout the simulation period.

The source-time functions output by the Material Point Method simulations contained significant long-period and quasi-static components, as expected for a large mass movement. Three component as displacement, velocity, and acceleration histories were recorded at the virtual receiver locations. In addition, the vector norms of the simulated fields were evaluated at each time step, and their maximum values over the complete simulation were stores at the free surface to generate shake maps and within the model volume to generate shake volumes.

Rather than obtaining velocity and acceleration by numerically differentiating the simulated displacement after time integration, was differentiated the source-time functions before the simulations. The original source histories were used for displacement, their first time derivatives for velocity, and their second time derivatives for acceleration. This required three simulations for each model realization, one for each output field, but allowed displacement,

velocity, and acceleration to be computed directly as the state variable of the wave equation. Because the second-order Newmark time-integration scheme is second-order accurate in the state variable itself, this approach reduced the additional numerical error that would otherwise be introduced by differentiating the simulated receiver and wavefield outputs during post-processing.

Figures 13 and 14 show frames of the result of wave propagation in terms of particle velocity and particle acceleration starting from time zero, that is, before the onset of the rupture, and at times of 2 seconds, 10 seconds, and 120 seconds, the latter being the end of the modeling. In the animations, the physical medium is represented in terms of shear wave velocity V_s. Cooler colors indicate lower shear wave values, while warmer colors indicate higher shear wave values. The propagation of surface waves is represented in yellow. The locations of the 44 virtual surface sensors are represented by magenta dots.

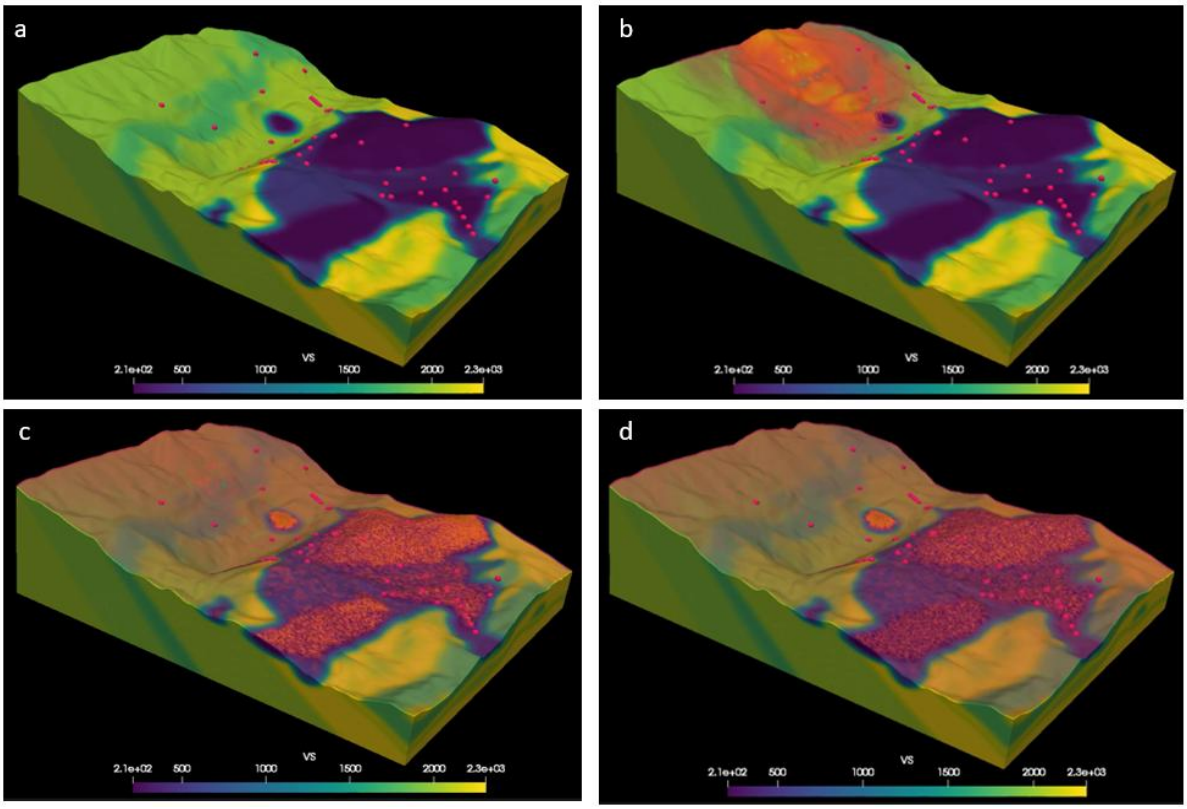


Figure 13: results of the particle velocity recorded in the medium at 0 seconds (figure a), 2 seconds (figure b), 10 seconds (figure c), and 120 seconds (figure d).

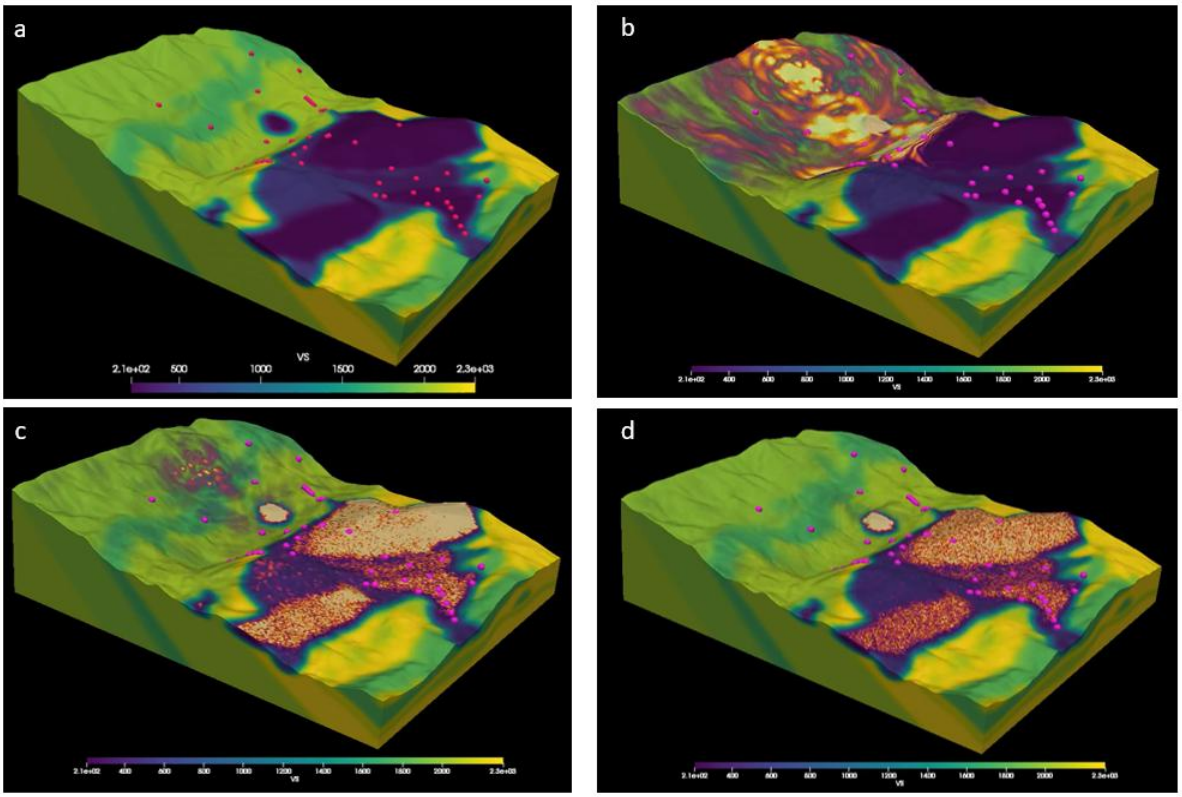


Figure 14: results of the particle accelerations recorded in the medium at 0 seconds (figure a), 2 seconds (figure b), 10 seconds (figure c), and 120 seconds (figure d).

The locations and maximum velocity values recorded in the pit, waste dump, dam embankment, and reservoir are shown in Figures 15, 16 and 17.



Figure 15: peak velocities observed in the pit.



Figure 16: peak velocities observed in the waste dump.

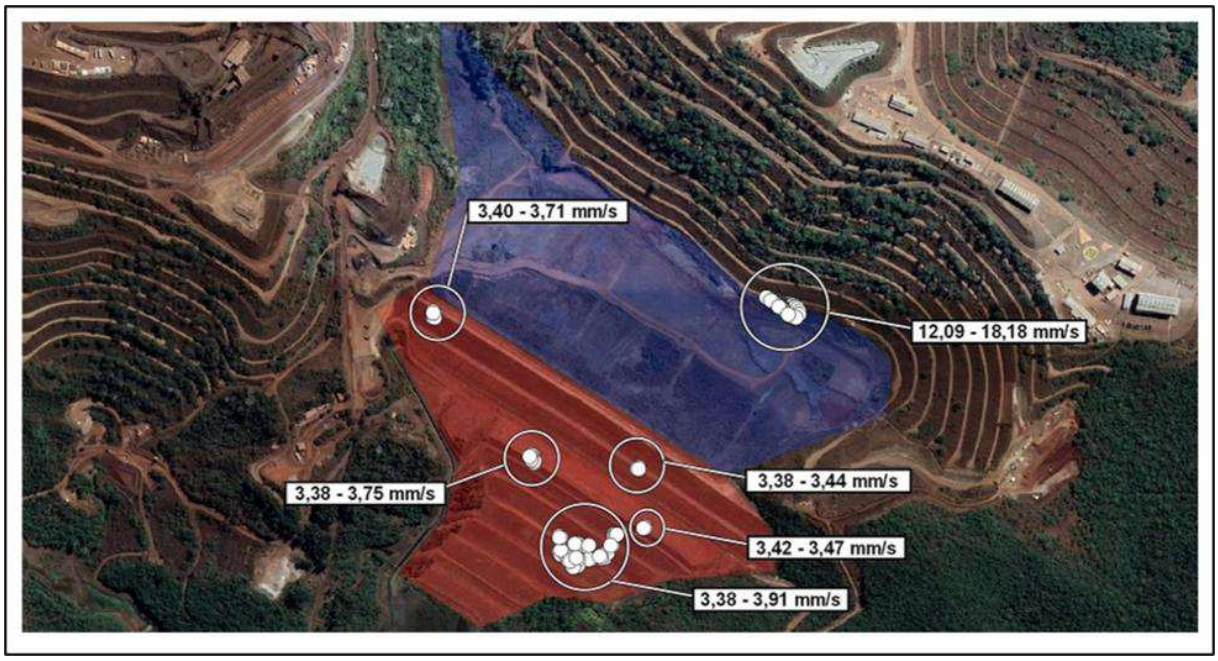


Figure 17: peak velocities observed in the dam (embankment in red and reservoir in blue).

The locations and maximum acceleration values recorded in the pit, waste dump, and the dam embankment and reservoir are shown in Figures 18, 19, and 20, respectively.



Figure 18: peak acceleration observed in the pit.



Figure 19: peak acceleration observed in the waste dump.



Figure 20: peak acceleration observed in the dam (embankment in red and reservoir in blue).

Figures 21 and 22 show the resulting maximum velocity and acceleration values, respectively, across the 44 surface virtual sensors considered in this study.

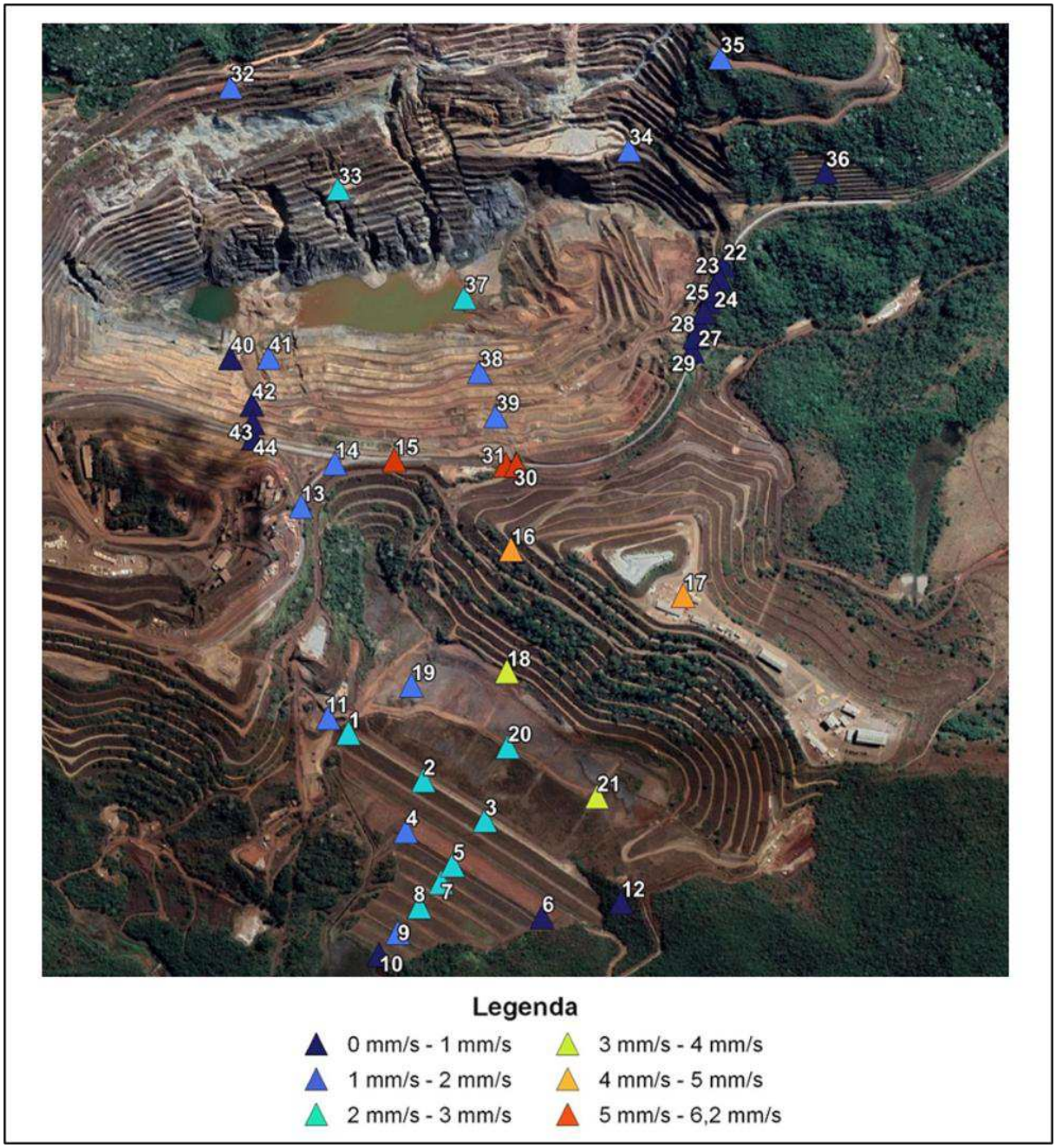


Figure 21: resultant velocity shakemap, representing the highest amplitudes recorded at each point of the material domain.

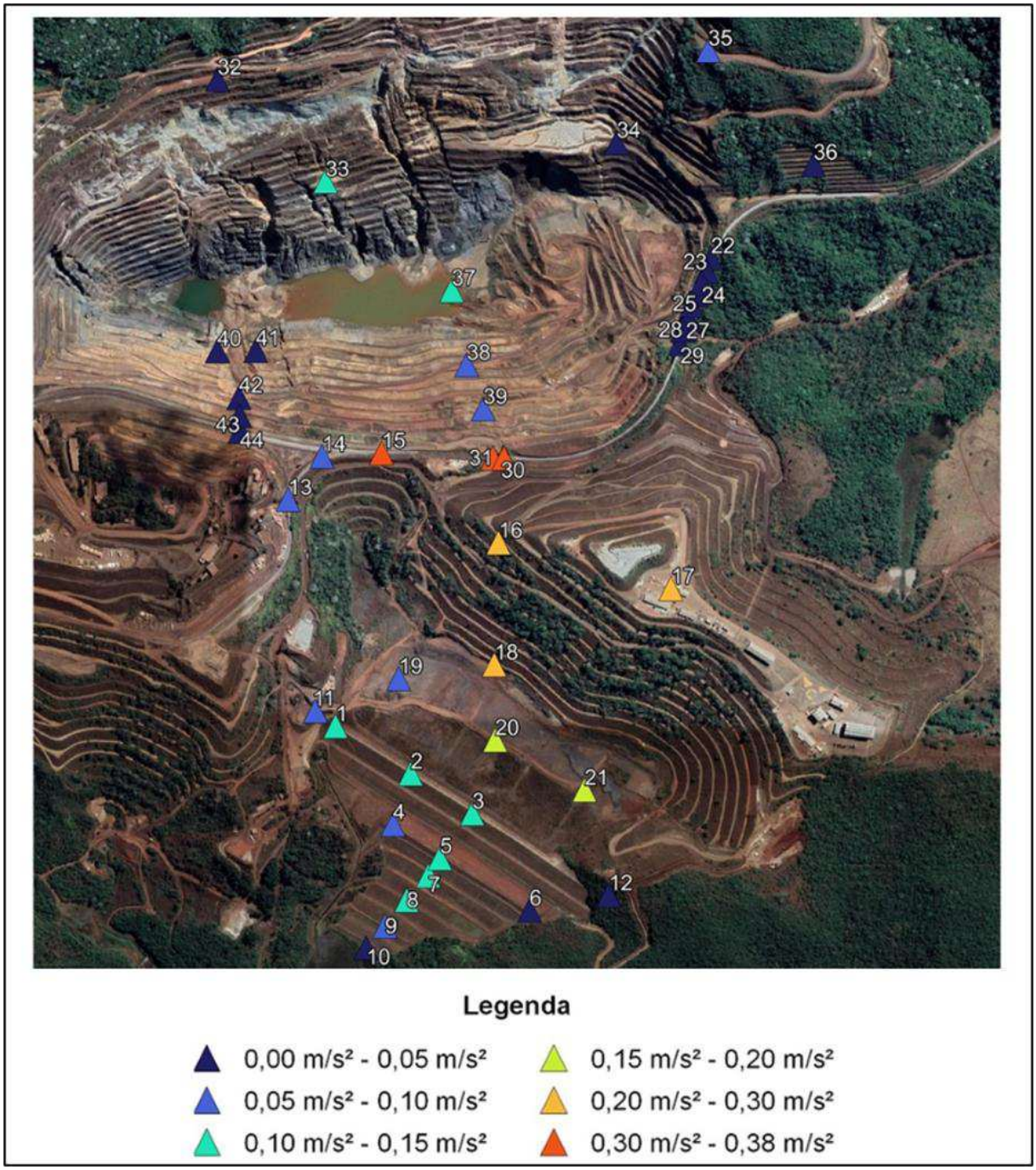


Figure 22: resultant acceleration shakemap, representing the highest amplitudes recorded at each point of the material domain.

The graphs in Figures 23 and 24 show the waveforms obtained in terms of velocity and acceleration obtained at sensor 3, which is located in the dam embankment. At this location, the waveform results were modeled for the surface, as well as for three other sensors located at depth.

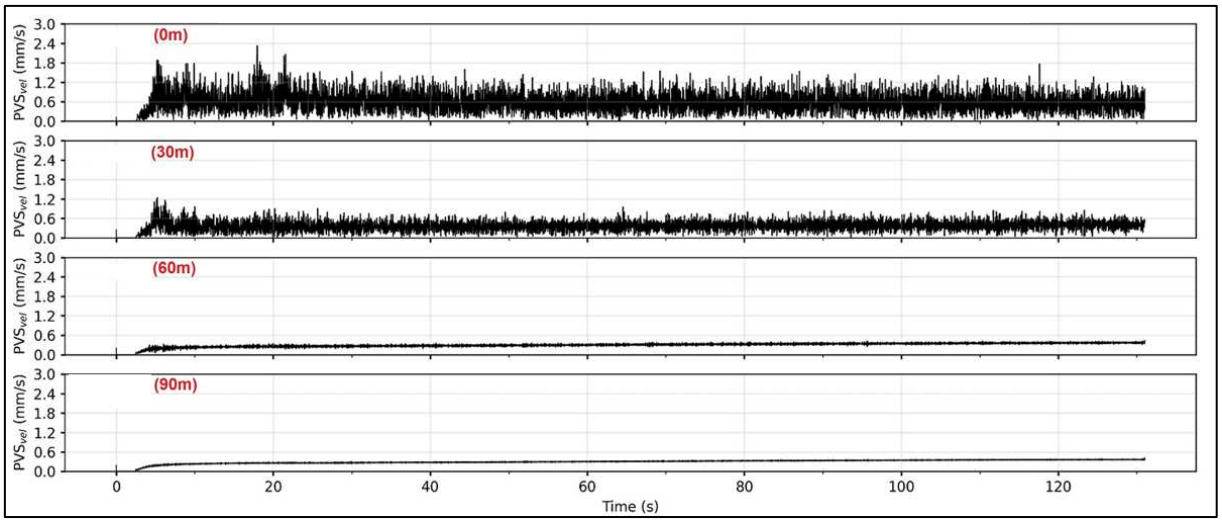


Figure 23: comparison between the velocity records from the surface sensor and those from the sensors at depth.

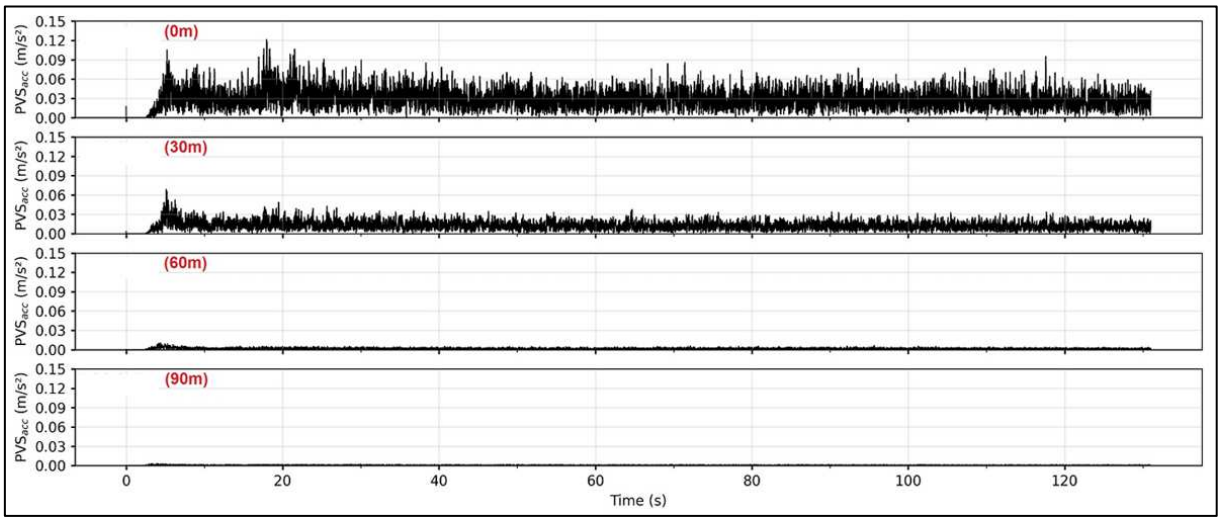


Figure 24: comparison between the velocity records from the surface sensor and those from the sensors at depth.

6. Discussions

Some recently published works, such as Feng *et al*. (2022), successfully coupled the Spectral Element Method (SEM) with the Material Point Method (MPM) to simulate wave propagation in the medium and simulate a massive landslide triggered by an earthquake. The present work performs the coupling in an inverse manner by coupling the MPM into the SEM.

From the perspective of continuum mechanics and elastodynamics, the model achieves conceptual validity, as it rigorously satisfies the governing equations of momentum conservation and wave propagation in heterogeneous media. Sensor arrays distributed throughout the domain successfully recorded distinct geometric attenuation patterns at both the surface and depth, validating the energy spreading formulations of the model. Furthermore, sharp lithological interfaces accurately simulated wave reflection and refraction processes, while significant wave amplification was quantified within upper geological layers characterized by lower impedance relative to the underlying basement rock.

However, it is crucial to emphasize that the obtained results, such as Peak Ground Acceleration (PGA) and Peak Ground Velocity (PGV) levels, are strictly site-dependent and event-

dependent. This implies that the computed vibrational response does not constitute a universal behavior, but rather a direct reflection of two local conditions: the mechanical characteristics of the rupture and the physical properties of the propagation medium. Within the scope of the dynamic source, represented by the MPM model, the temporal signature and amplitude of the recorded forces depend critically on the fault kinematics, the mobilized mass, the adopted basal friction coefficient (μ), and the biplanar failure plane geometry. Any variation in these parameters substantially modifies the energy transmitted from the collapsed mass to the medium.

Outside the active landslide zone modeled by the Material Point Method (MPM), the surrounding medium is treated as strictly elastic, and intrinsic material damping is omitted due to regional parametric complexity and a scarcity of experimental calibration data. Mechanically, the absence of elastoplasticity in the medium and an attenuation profile (Q-factors) prevents energy consumption through plastification or material damping, meaning the current model propagates high frequencies over longer distances and yields higher wave amplitudes than a possible real-world scenario.

Therefore, it is concluded that the presented numerical framework is methodologically robust and suitable for assessing large-scale hypothetical scenarios, with the technical caveat that its resulting ground-shaking maps and spectra are restricted to the analyzed mine site, precluding their extrapolation to other locations without a comprehensive recalibration of both the medium properties and the source geometry.

7. Conclusion

In this study, a fully deterministic physics-based numerical framework was developed to simulate and quantify site-specific seismic ground vibrations originating from a potential ten-million-ton mass collapse within an open pit mine. By successfully coupling large deformation geomechanics with structural wave propagation, this research introduced a novel inverse pathway (MPM to SEM). Unlike conventional approaches that model earthquake-induced landslides (SEM to MPM), this framework utilizes the dynamic contact forces generated during a hypothetical mass collapse in to bottom pit applying the Material Point Method (MPM) to act as the primary seismic source driving regional wave propagation in the Spectral Element Method (SEM).

The main conclusions of this work are summarized as follows:

1. Inverted computational pathway validation: the coupling mechanism between MPM and SEM proved to be a consistent, realistic, and mathematically representation of wave behavior within complex mining medium. The methodology successfully captured the transition from macroscopic slope deformation to structural wave generation without relying on empirically pre-defined seismic source functions.

2. Ground motion quantifications: through 3D numerical modeling, the framework successfully generated high-resolution spatial velocity and acceleration shakemaps across the entire area of interest. These results demonstrate that integrating large-deformation mechanics with regional elastic wave propagation allows for a comprehensive evaluation of near-field ground shaking induced by non-tectonic mass failures.

3. Topographic and geological influence: the integration of real 3D topographies and multi-layered geological medium within the SEM scale allowed for an accurate simulation of geometric wave effects, highlighting areas susceptible to localized amplification around the open pit slopes.

In the future, comprehensive parametric and sensitivity analyses will be conducted to investigate how critical geomechanical properties (such as strain-softening parameters, peak/residual friction angles, and cohesion) dominantly control mass displacement and the subsequent the energy of the induced seismic waves. Additionally, the validated framework can be leveraged to assess the dynamic impacts of landslide induced vibrations on surrounding environments, paving the way for comprehensive risk analyses and vulnerability assessments of critical civil and geotechnical infrastructure.

8. Acknowledgements

The authors express their gratitude to the Federal University of Ouro Preto (UFOP) and the Núcleo de Geotecnia (NUGEO) for providing the institutional support required to develop this research.

9. Declarations

Funding and/or Conflicts of interests/Competing interests: the authors declare that they have no competing financial interests or personal relationships that could have appeared to influence the work reported in this paper.

Ethics approval and consent to participate: not applicable.

Consent for publication: not applicable.

10. Bibliographic References

Aki, Keiiti; Richards, Paul G. Quantitative Seismology. 2. ed. Sausalito, CA: University Science Books, 2002.

Ammon, Charles H.; Velasco, Aaron A.; Lay, Thorne; Wallace, Terry C. Foundations of Modern Global Seismology. 2. ed. [S. l.]: Academic Press, 2021.

Clayton, R. and Engquist B., “Absorbing Boundary Conditions for Acoustic and Elastic Wave Equations,” Bulletin of the Seismological Society of America, 67, 1529–1540, 1977.

Eikmeier, C. N., Fernández, F., Bezerra, T. M. B., Machado, D. M., Figueiredo, R. P., Paganin Neto, M., Ribeiro, E. L., Delveaux, J. P., Nogueira, C. A., Euzébio, C. S., & Vale, L. M. de A. (2025). Sensitivity analysis of rock slope stability under water level variation using 3D Material Point Method (MPM) simulations. Tetra Tech South America; Universidad Católica del Norte, Departamento de Ingeniería Civil; Federal University of Ouro Preto.

Fernandéz, F. Modelagem numérica de problemas geotécnicos de grandes deformações mediante o método do ponto material. 2020. Tese (Doutorado em Engenharia Civil) — Pontifícia Universidade Católica do Rio de Janeiro, Rio de Janeiro, 2020.

Feng, K., Huang, D., Wang, G., Jin, F., & Chen, Z. (2022). Physics-based large-deformation analysis of coseismic landslides: A multiscale 3D SEM-MPM framework with application to the Hongshiyan landslide. *Engineering Geology*, 297, 106487. https://doi.org/10.1016/j.enggeo.2021.106487.

Fichtner, Andreas. Full Seismic Waveform Inversion. Berlin: Springer-Verlag, 2011

Gualtieri, L.; Ekström, G. Seismic reconstruction of the 2012 palisades rockfall using the analytical solution to lamb's problem. Bulletin of the Seismological Society of America, v. 107, n. 1, p. 63–71, 2017. DOI: 10.1785/0120160238.

Igel, Heiner. Computational Seismology: A Practical Introduction. Oxford: Oxford University Press, 2017.

Kramer, S. L., Stewart, J.P., 2024. Geotechnical Earthquake Engineering, 2.ed., Taylor & Francis, CRC Press.

Komatitsch D., Tromp J., 1999. Introduction to the spectral element method for three-dimensional seismic wave propagation. Geophysics J Int 139(3):806–822.

Kosloff, R., & Kosloff, D. Absorbing Boundaries for Wave Propagation Problems. Journal of Computational Physics, v. 63, n. 2, p. 363–376, 1986.

Milner, K. R., Shaw, B.E., Goulet, C. A., Richards-Dinger, K.B., Callaghan, S., Jordan, T.H., Dieterich, J. H., Field, E. H. 2021.Toward Physics-Based Nonergodic PSHA: A Prototype Fully Deterministic Seismic Hazard Model for Southern California. Bulletin of the Seismological Society of America. DOI:10.1785/0120200216.

Nairn, John A. Material point method calculations with explicit cracks. Computer Modeling in Engineering & Sciences (CMES), v. 4, n. 6, p. 649-664, 2003. DOI: 10.3970/cmes.2003.004.649

Shearer, Peter M. Introduction to Seismology. 2. ed. Cambridge: Cambridge University Press, 2009.

Slawinski, Michael A. Seismic Waves and Rays in Elastic Media. St. John's: Department of Earth Sciences, Memorial University of Newfoundland, 2003.

Sulsky, Deborah; Hou, Shun-Ji; Schreyer, Howard L. Application of a particle-in-cell method to solid mechanics. Computer Physics Communications, v. 87, p. 179-196, 1994.

Pankow, K.L., Moore, J.F., Hale, J.M., Koper, K.D., Kubacki, T., Whidden, K. M., McCarter, M.K. Massive landslide at Utah copper mine generates wealth of geophysical data. College of Mines and Earth Sciences, University of Utah, Salt Lake City, 2012.

DOI:10.1130/GSATG191A.1.

Zhang, Xiong; Chen, Zhen; Liu, Yan. The Material Point Method: A Continuum-Based Particle Method for Extreme Loading Cases. Amsterdam: Academic Press/Elsevier; Beijing: Tsinghua University Press, 2017. 527 p. ISBN 978-0-12-407716-4.

Zhao, Lianheng; Qiao, Nan; Huang, Dongliang; Zuo, Shi; Zhang, Zijian. Numerical investigation of the failure mechanisms of soil–rock mixture slopes by material point method. Computers and Geotechnics, v. 150, art. 104898, oct. 2022.

Zheng, L., Zhao, Q., Milkereit, B., Grasselli, G., & Liu, Q. (2019). Spectral-element simulations of elastic wave propagation in exploration and geotechnical applications. *Geophysical Journal International, 216*(3), 1799–1817. https://doi.org/10.1093/gji/ggy522

Supplementary Files

This is a list of supplementary files associated with this preprint. Click to download.

- Runout.mp4
- Velocityseismicwaves.mp4
- Accelerationseismicwaves.mp4